Analytical modelling of CO_2 reduction in gas-diffusion electrode catalyst layers

Blake, J. W.; Padding, J. T.; Haverkort, J. W.

Important note
To cite this publication, please use the final published version (if applicable).
Please check the document version above.

Analytical modelling of CO_2 reduction in gas-diffusion electrode catalyst layers

J.W. Blake*, J.T. Padding, J.W. Haverkort

Department of Process and Energy, Delft University of Technology, Leeghwaterstraat 39, 2628 CB Delft, the Netherlands

ABSTRACT

The electrochemical reduction of CO_2 on planar electrodes is limited by its prohibitively low diffusivity and solubility in water. Gas-diffusion electrodes (GDEs) can be used to reduce these limitations, and facilitate current densities orders of magnitude higher than the limiting current densities of planar electrodes. These improvements are accompanied by increased variation in the local environment within the cathode, with significant effect on Faradaic efficiency. By developing a simple and freely available analytical model of a cathodic catalyst layer configured for the production of CO, we investigate the relationships between electrode reaction kinetics, cell operation conditions, catholyte composition and cell performance. Analytical methods allow us to cover parameter ranges that are intractable for numerical and experimental studies. We validate our findings against experimental and numerical results and provide a derivation and implementation of the analytical model.

© 2021 The Authors. Published by Elsevier Ltd.
This is an open access article under the CC BY license (http://creativecommons.org/licenses/by/4.0/)

1. Introduction

The electrochemical reduction of CO_2 has seen much attention in recent years for its potential as a panacea solution to the limitations of renewable energy sources [1–4]. Electrochemical CO_2 reduction (CO2R) can yield a variety of products such as formate [5,6], syngas [7] and ethylene [8], which can serve as carbon-neutral feedstock for the chemical industry or as scalable chemical energy storage [9]. However, the process is prohibited by the low solubility [10] ($\lesssim$ 30 mM) and diffusivity of CO_2 in aqueous electrolytes at ambient conditions, the low Faradaic efficiency, and the poor utilisation of supplied CO_2, resulting in the limiting CO2R current density on planar electrodes (10–30 mA cm^{-2}) [11] being far lower than the economically viable minimum. These limitations have been addressed in recent years through the adoption of gas-diffusion electrodes (GDEs) [12], which greatly reduce the boundary layer thickness and enable current densities orders of magnitude higher than what is possible on planar electrodes.

Despite historical success [13] in the development of GDE structures for use in proton exchange membrane fuel cells (PEMFCs) [14], there are many design parameters that must be optimised for GDEs in CO2R cells [15]. A GDE consists of a dry macrop-

orous gas-diffusion layer (GDL) through which the CO_2 diffuses and electronic current can flow, a thin hydrophobic microporous layer (MPL) that acts as a bed for the catalyst layer while preventing electrolyte flooding into the GDL [16], and a catalyst layer (CL) in which embedded catalyst particles provide active sites for electrochemical reduction (see Figure 1). The CL usually consists of catalyst particles deposited onto the (MPL), creating a thin microporous structure into which both electrolyte and CO_2 can enter. However, the performance of a true GDE is seldom attained, as in practice the CL commonly becomes highly saturated with liquid electrolyte. The three-phase interface retreats to the MPL and can in places even break through into the GDL in flooding events.

Full cell setups also vary outside of the cathode. This work covers a flow cell, in which electrolyte flows between a cathode performing CO2R, in competition with a simultaneous hydrogen evolution reaction (HER), and an anode performing the oxygen evolution reaction. Following PEMFC setups, it is common to include an ion exchange membrane between the anode and cathode. Experiments have been performed with bipolar, anion, and cation exchange membranes, as well as with full membrane electrode assemblies replacing one or both of the aqueous electrolyte channels. These different setups can better control the transport of ions, but can lead to issues with conductivity and water management. Although the catalysts and designs may vary for the oxygen evolution reaction taking place at the anode, these variations are often neglected as a non-limiting process with no effect on cathodic FE.

---

* Corresponding author.
    E-mail address: J.W.Blake@tudelft.nl (J.W. Blake).
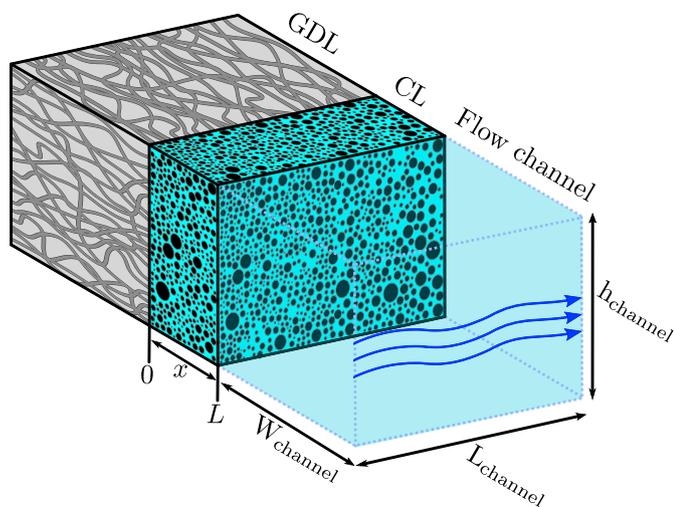
Fig. 1. 3D cross-section of the GDE cathode, showing the electrolyte flow channel and flooded CL next to the dry GDL. The numerical CL domain considered spans from $x = 0$ at the GDL boundary to $x = L$ at the flow channel boundary, where L is the CL thickness (not to scale).

Different catalysts can, however, lead to different reactions at the cathode, which may have a distribution of gas or liquid products.

There are a number of factors limiting the performance of the CL. Despite a large reduction in mass-transfer resistance compared to planar electrodes, the CO_2 concentration drop within a CL fully flooded with electrolyte remains large at high current densities [17]. Although the resistance can be further reduced by maintaining gas channels within the CL itself [18], the multiphase boundaries are difficult to control as flooding resistance has been shown to vary with current density [19]. Furthermore, the Faradaic efficiency (FE) towards desired products is impacted negatively by the hydrogen evolution reaction on the electrode [20]. The competing HER is suppressed in high pH electrolytes [21], but high OH^- concentrations drive the carbonate equilibrium reactions to chemically consume CO_2 to form bicarbonate and carbonate at a rate comparable to that of the electrode reaction. At high current densities this parasitic chemical loss of dissolved CO_2 can account for over 50% of the total CO_2 consumption. This reduces reactant utilisation and leads to a reduction in CO_2 solubility due to the salting-out effect in the resulting high ionic-strength electrolyte [22]. High concentrations of carbonate can also lead to salt precipitation and loss of hydrophobicity in the MPL and GDL, leading to detrimental liquid breakthrough and flooding. In cells with an anion-exchange membrane, it is also possible for carbonate to cross over to the anode, along with a significant portion of the liquid products [23], and re-evolve [24,25].

In this work we derive an analytical approximation of cathodic CL dynamics and use it to determine the effect of carbonate on cell performance and how the state of the equilibrium reactions can be influenced by cell parameters. The model uses Ag catalyst particles as their high selectivity towards CO and H_2 [26–29] allows us to neglect products of further reduction that require additional reaction parameters [30]. The benefit of analytical predictions is in their versatility: one can cover vast parameter spaces with ease and parametric studies do not require long computational or experimental time investments.

2. Model

2.1. Theory

The CL is modeled as a 1D domain in the plane-perpendicular direction, as shown in Figure 2, with mass-transfer boundary con-

ditions determined by the electrolyte channel properties and GDL gas phase interface. The porous medium is assumed to be homogeneous and fully flooded with electrolyte at a liquid fraction of ϵ. Although earlier studies proposed that the reaction takes place only at a triple-phase boundary [31,32], recent studies have determined that it is more likely to occur at a solid-liquid boundary [33], and flooded CLs can still exhibit high current densities. Local variation in structure is difficult to categorise and is neglected, though studies show that the effects of variation can be significant [34–36]. The volumetric reactive surface area, a, is assumed constant throughout the CL and can be correlated with further CL structure properties (SI.1.1.2). Diffusion of aqueous species through the medium is corrected for porosity and tortuosity through the Bruggeman relation $D_{eff} = D\epsilon^{\frac{3}{2}}$. We assume that all species remain in an aqueous state within the CL, neglecting the effects of bubble formation and bubble-induced voltage instability [37].

The GDL acts as a source of CO_2 at pressure p_{CO_2}. Other gaseous species in the GDL are neglected, and while CO and H_2 products can escape freely into both the GDL and the electrolyte channel they are assumed to have negligible effect on CO_2 transport and chemical equilibria. As an important limiting factor, the transport of CO_2 from the GDL to the CL is based on Henry's Law with the solubility of CO_2 in the electrolyte corrected for ionic content through the Schumpe [38] extension to the Sechenov [22] equation. The electrolyte channel consists of a potassium bicarbonate ($KHCO_3$) solution in a plane-parallel Poisueille flow with average velocity v, with carbonate equilibria determined from the electroneutrality condition and carbon conservation and corrected for ionic strength and temperature. In-plane effects have been shown to be significant enough to lead to a drop in current density in the streamwise direction, from 450 mA cm^{-2} to <300 mA cm^{-2}, in addition to large streamwise pH gradients [39]. Although this cannot be fully captured in a 1D model, we expect the majority of the variation to be due to the development of the electrolyte ionic concentration profiles, namely OH^-, bicarbonate and carbonate, from a thin developing concentration boundary layer near the inlet of the electrolyte channel to a fully developed concentration profile downstream. This variation, along with the possibility for a developing flow profile, is accounted for in the determination of electrolyte boundary conditions. More information on the solubility and boundary conditions can be found in SI.1.2.2.

As Ag catalysts are highly selective towards CO and H_2, we neglect other electrode reactions. Furthermore, the cathodic potentials at relevant current densities are sufficient for us to discard anodic branches of the electrode reactions and assume Tafel kinetics, with a first-order dependence on CO_2 concentration for the CO evolution reaction [40] and a concentration independent basic reaction pathway for HER [41] for constant water content.

$$CO_2 + H_2O + 2e^- \rightarrow CO + 2OH^-, \qquad E^0_{CO} = -0.11 \text{ V},$$
$$2H_2O + 2e^- \rightarrow H_2 + 2OH^-, \qquad E^0_{H_2} = 0 \text{ V},$$
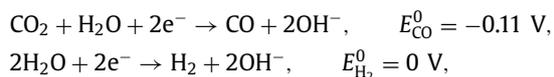
with current densities

$$i_{CO2R} = -i_{0,CO2R} \frac{[CO_2]}{[CO_2]_{ref}} \exp\left(\frac{-\eta_{CO2R}}{b_{CO2R}}\right) \qquad (1)$$

$$i_{HER} = -i_{0,HER} \exp\left(\frac{-\eta_{HER}}{b_{HER}}\right), \qquad (2)$$

where i_0, η and b are the exchange current densities, overpotentials and Tafel slopes respectively. The Tafel slope is related to the charge transfer coefficient α by $b = \frac{RT}{F\alpha}$ where F and R are Faraday's constant and the universal gas constant respectively. Geometric current densities; that is, current density per unit external CL area, can be determined by integrating the superficial current densities described in (1) and (2) along the thickness of the CL and multiplying by the volumetric surface area, a. Our domain consists
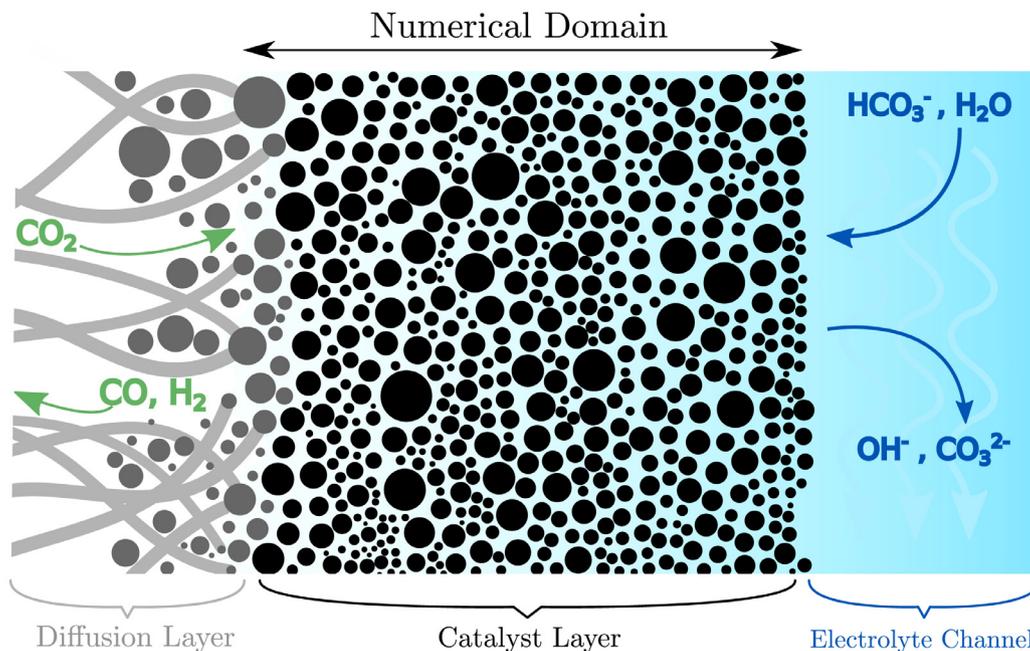
Fig. 2. The numerical model covers a 1D plane-perpendicular domain of the catalyst layer, with boundaries at the microporous layer and GDL (left) and electrolyte flow channel (right). The blue-filled domains represent liquid phase portions and clear domain represents gas phase. At the far right side of the electrolyte channel will be a membrane and anode surface.

of only a single CL, so the ohmic drops across the remainder of the cell are not included here. Furthermore, the Wagner number in the CL, which is the ratio of solution and polarisation resistance, is large (Wa $= \frac{\kappa b}{i_0 L} \approx 10^4$) for typical values of the electrolyte conductivity κ, meaning that ohmic drops are negligible and the majority of the ohmic drop of the full cell occurs outside of the CL. The assumptions of Tafel kinetics are generally valid when the total Butler-Volmer current density significantly exceeds the exchange current density, which is true for both considered reactions at relevant CO current densities of > 1 mA cm^{-2}. Furthermore, any effect on local reaction environment in the low overpotential regime would be outweighed by the buffering effect of the homogeneous chemical reactions. These alkaline carbonate equilibrium reactions are modelled kinetically in the CL, closed with the assumption of arbitrarily fast water dissociation,

$$CO_2 + OH^- \underset{k_{-1}}{\overset{k_1}{\rightleftharpoons}} HCO_3^-, \qquad K_1 = 10^{7.69} \text{ M}^{-1}, \qquad (3)$$

$$HCO_3^- + OH^- \underset{k_{-2}}{\overset{k_2}{\rightleftharpoons}} H_2O + CO_3^{2-} \qquad K_2 = 10^4 \text{ M}^{-1}, \qquad (4)$$

$$H_2O \longleftrightarrow H^+ + OH^- \qquad K_w = 10^{-14} \text{ M}^2, \qquad (5)$$

where k_n and k_{-n} are the forwards and backwards rate coefficients respectively, and $K_n = \frac{k_n}{k_{-n}}$ are the equilibrium constants. The acidic carbonate equilibrium reactions are considered kinetically in the numerical model, but are neglected in the analytical model. More information on the quantitative justification for this can be found in SI.3.1.

2.2. Numerical method

A numerical model was created in COMSOL Multiphysics, solving species transport and tertiary current distribution through the Nernst-Planck equation. Steady state solutions were determined using the MUMPS solver with geometrically scaled node spacing to improve resolution at the boundaries. Electrode geometry and operational parameters, were chosen to mimic the experimental setup of Verma et. al. [29]. The electrolyte carbonate equilibrium

state was determined from experimentally reported pH and concentration. Further information regarding the scope and limitations of the numerical model can be found in SI.1, SI.5.

2.3. Analytical solution

The main contribution of this work is an approximate analytical solution. This solution was determined by decoupling ionic species from CO_2, solving the reaction-diffusion equation for CO_2 along the CL. Ionic concentrations were averaged within the CL, whereas the CO_2 concentration was determined by solving the reaction-diffusion equation,

$$[CO_2] = [CO_2]_{DL} \frac{\cosh\left(M_T(1 - \frac{x}{L})\right)}{\cosh\left(M_T\right)}, \qquad (6)$$

$$M_T = \sqrt{\frac{L^2 k}{D_{CO_2}^{\text{eff}}}}, \qquad (7)$$

$$k = \epsilon k_1 [OH^-] + \frac{a}{2F} \frac{i_{0,\text{CO2R}}}{[CO_2]_{\text{ref}}} \exp\left(\frac{-\eta_{\text{CO2R}}}{b_{\text{CO2R}}}\right) \qquad (8)$$

where $[CO_2]_{DL}$ is the CO_2 concentration at the GDL-CL boundary, M_T is the Thiele [42] modulus and k is the total volumetric CO_2 reaction rate, which is the sum of volumetric electrode reaction rate determined from the current density in (1) and chemical reaction rate (3).

By only considering average ionic concentrations we arrive at a simple mass balance equation, equating the boundary flux from the electrolyte channel with the total chemical reaction rate in the CL and, in the case of OH^-, electrode reaction rate, (SI.2.2). However, the nonlinear dependencies of OH^- on the Nernstian equilibrium potential and of ion concentrations on CO_2 solubility and thus $[CO_2]_{DL}$ led to an analytically intractable system of equations, so the ionic system was decoupled and solved approximately to then be recombined with the Thiele solution. A derivation and method of reproduction can be found in SI.2.2 and SI.2.3, respectively.
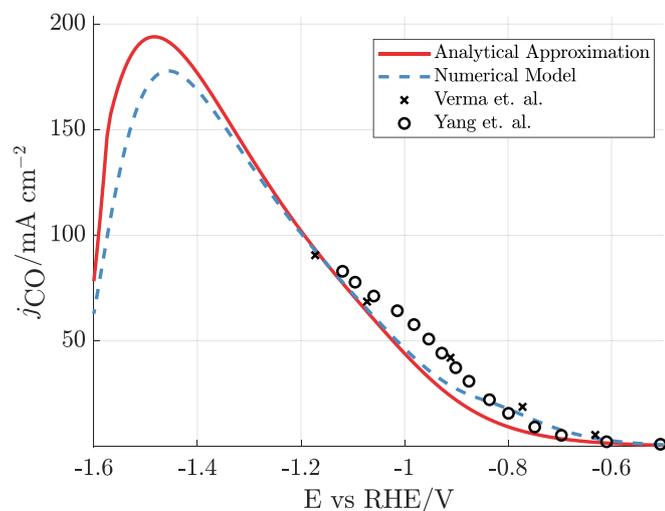
Fig. 3. Numerical and analytical models compared to experimental data from Verma et. al. [29] for a KHCO$_3$ concentration of 1 M and flow rate of 0.5 ml min^{-1}. Electrolyte species concentrations were determined directly from experimentally reported pH rather than determined through the analytical model. An additional set of experimental data from Yang [49] is included, in which a similar experimental setup is used. More information can be found in SI.7.1.

Table 1
Parameters used in the numerical and analytical models. Equilibrium potentials are expressed vs RHE.

Parameter	Value	Unit	Ref.
α_{CO}	0.44	[-]	[43]
α_{H_2}	0.36	[-]	[43]
E^0_{CO}	−0.11	V	[44]
$E^0_{H_2}$	0	V	[44]
L	3.81×10^{-6}	m	[45]
a	3×10^7	m^{-1}	[46]
ϵ	0.5	[-]	
T	293.15	K	
p_{CO_2}	1	atm	
$w_{channel}$	1.5×10^{-3}	m	[47]
$L_{channel}$	0.02	m	[47]
$h_{channel}$	5×10^{-3}	m	[47]
q_{flow}	0.5	ml min^{-1}	[48]

3. Results

The analytical model was implemented in spreadsheet form for ease of use, and is freely available from the SI. The following analytical plots were generated using the analytical model and verified against further numerical simulations. Figure 3 shows a comparison between the CO current densities predicted by the analytical approximation and the numerical and experimental results. Between −0.4 V and −0.8 V we see an exponential relationship between potential and current, indicating a kinetically (activation overpotential) limited regime governed predominantly by the Tafel equation. The flattening curve with more negative potential is indicative of the drop in aqueous CO$_2$ concentration, with the peak current density being attained when the parasitic chemical reaction (3) and CO$_2$ transfer limitations combine to outweigh increasing overpotential. At post-peak potentials, unhindered HER leads to a high ionic strength catholyte with poor solubility, which readily consumes CO$_2$ to reduce the pH.

The approximation is an excellent match for the numerical model, with small discrepancies arising only at −0.7 V and in the neighbourhood of the peak current density. These discrepancies are due to term neglections in the simplified homogeneous reactions used to predict pH in Eq. (SI:44) and degradation of the approximation of carbonate concentration in Eq. (SI:67) respectively. The latter error remains small for potentials less negative than the potential at peak current density but can increase at very negative potentials, as is observable in the −1.4 to −1.5 V vs RHE range in Fig. 3. The analytical solution begins to degrade for parameter combinations that allow ion concentrations large enough to necessitate inclusion of more detailed ionic effects, or for parameter combinations that allow large ion concentration gradients to develop within the CL, which prohibit the use of concentration averages in the model. The former can arise at potentials lower than −1.4 V vs RHE or with low electrolyte flow rate (<0.5 ml min^{-1}) and the latter can arise for large CL thicknesses (>100 μm) when paired with low electrolyte flow rates.

In Fig. 4a we plot CO current density against CL thickness at multiple cathode potentials (coloured lines) and at the optimal potential (dashed black line): the thickness dependent potential which achieves maximum CO current density. This optimal poten-

tial is also seen to be dependent on the electrolyte channel flow rate in Fig. 4b, and in general is dependent on every parameter in Table 1. This optimum can be clearly seen to vary in Fig. 4a as it intersects the other potential curves for different thicknesses. The specific value of the optimal potential is most easily extracted by applying a simple root finding method to the data sets provided by the analytical approximation. We assume that the ohmic drop is small compared to the Tafel slope for the considered CL thicknesses so that mass transfer determines optimal performance [50]. Thicker CLs have more surface area available for reaction, but suffer from poorer mass transfer due to longer diffusion distances. A thick CL exhibits relatively high current densities at weak potentials but poor peak current density, as the mass transfer limitations begin to occur at lower current densities and are more severe. By contrast, a thin CL benefits from a shorter diffusion distance, meaning that aqueous CO$_2$ concentrations can remain relatively high at high current densities. As the Tafel slope of the CO2R reaction is lower than that of HER, this allows for much improved Faradaic efficiency for the same CO current density in a thinner CL, albeit at a more negative potential. The combined reduction in OH$^-$ generation from HER and increase in CO2R overpotential lead to higher CO$_2$ utilisation and lower ionic strength compared to a thicker CL. This delays the onset of solubility and parasitic reaction limitations, allowing the thinner CLs in Fig. 4a to attain higher limiting CO densities.

Figure 4b shows the impact of electrolyte flow rate on current density for a range of potentials. We reflect literature trends by utilising flow rate as an independent variable, but it is important to note that the electrolyte boundary conditions are also dependent on channel geometry. Nonetheless, Fig. 4b shows the importance of flow rate in attaining high current densities in regimes limited by salting out effects. The flow channel boundary mass transfer is improved at higher flow rates, facilitating faster removal of OH$^-$ and carbonate while replenishing bicarbonate, all of which serve to decrease the pH in the CL. This improves CO$_2$ solubility and reduces parasitic reaction rate, increasing CO$_2$ concentration and current density. By contrast, increasing flow rate has only a small effect at −0.8 V and −1 V in Fig. 4b, as in both cases current density is limited by a small activation overpotential and neither mass transfer limitations nor ionic effects play a significant role.

Figure 5a further shows how closely the analytical approximation of CO$_2$ concentration matches the numerical concentration. The deviation at −0.8 V is due to the analytical assumption of zero CO$_2$ flux through the electrolyte boundary. This discrepancy consequently shows precisely how much CO$_2$ concentration is reduced through direct loss to the electrolyte channel and how this loss has a negligible effect at relevant potentials. However, this loss is positively correlated with electrolyte flow rate, so at potentials lower
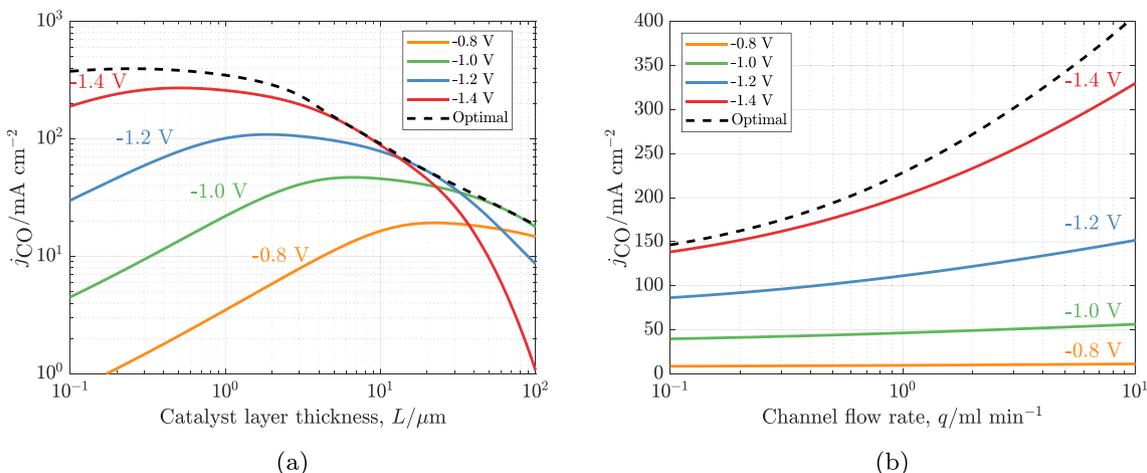
Fig. 4. Analytical CO current density against CL length for fixed electrolyte flow rate 0.5 ml min^{-1} (a), and against electrolyte flow rate (b), with curves for different potentials ranging from -0.8 to -1.4 V vs RHE. Dashed black lines indicate the maximum current density predicted by the model for the chosen parameters. Note that for all addressed CL thicknesses there is a potential at which its performance exceeds all other thicknesses, and vice versa. Details of flow channel geometry are available in Table 1, with which one can convert to flow velocity or flow rate for a channel with different cross-sectional area.
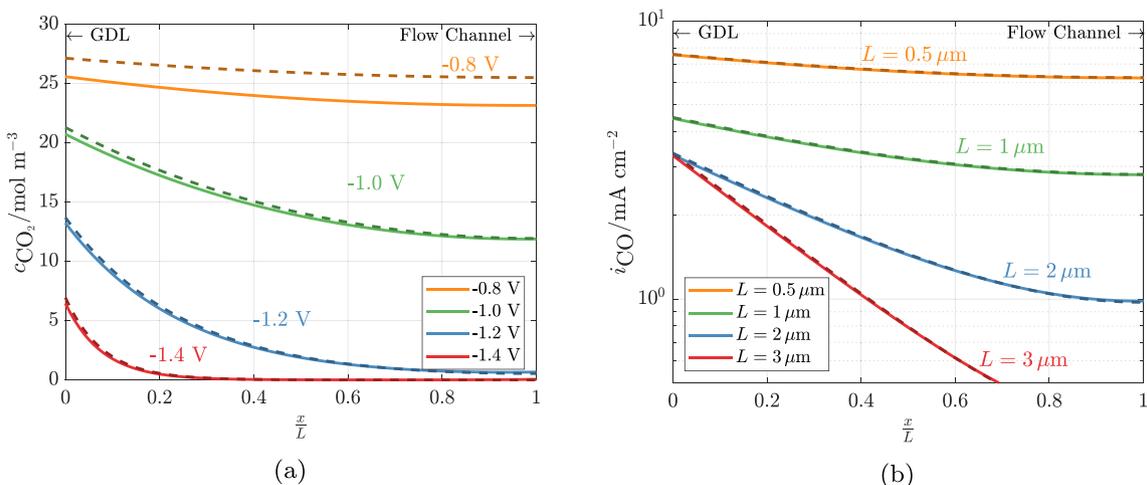
Fig. 5. Analytical (dashed) and numerical (lined) concentration plots for CO_2 along the length of the CL at varying potentials (a), and local current density distributions at a geometric current density of 100 mA cm^{-2} for different CL thicknesses (b). The analytical prediction of CO_2 concentration variation within the CL is shown to be an excellent match with numerical results at large potentials and similarly for the analytic current density distribution at 100 mA cm^{-2}.

than -0.8 V an increase in flow rate can cause a large enough CO_2 loss to the channel to lead to a reduction in current density and CO_2 utilisation.

Due to the low variation of overpotential within the CL, the local superficial current density distribution follows the CO_2 concentration. Fig. 5b shows that for the same geometric current density, thinner CLs will have more uniform current density distributions, whereas thicker CLs will exhibit a much less uniform distribution, with the majority of the reaction taking place close to the GDL boundary.

The average chemical species concentrations in the CL are shown in Fig. 6b, where more negative potentials lead to increasing pH and carbonate concentration with a corresponding drop in CO_2 and bicarbonate concentration. For all potentials considered this way the equilibrium reaction (4) remains in equilibrium, while reaction (3) is forced out of equilibrium at high current densities by rapid depletion of bicarbonate. This causes the back reaction of (3) to be negligible and it becomes practical to view and analytically approximate the parasitic chemical reaction as a direct conversion of CO_2 to carbonate, consuming $2OH^-$, rather than a two-step process, as seen in Eq. (SI:39-42). Influent bicarbonate

and CO_2 are both consumed increasingly rapidly as pH increases, producing increasing amounts of carbonate.

The latter effects are shown in Fig. 6b, where at large negative potentials up to 45% of CO_2 entering the CL is not reduced to CO. As determined earlier and shown in Fig. 5a, the loss of CO_2 to the electrolyte channel is negligible at these potentials, so this loss of CO_2 can be directly attributed to chemical reaction with OH^-. The corresponding increase in ionic strength leads to a large reduction in solubility. This solubility reduction is observable in Fig. 5a, as it is the primary cause of the reduction in CO_2 concentration at the GDL boundary, and at potentials more negative than -1.5 V in Fig. 3, where it is the cause of the fall in CO_2 current density as the system becomes entirely mass transfer limited. It is possible for solubility to be reduced to such a degree that even the carbonate concentration begins to peak and fall at further negative potentials, as less CO_2 is available for consumption. The analytical approximation degrades in this regime and underestimates the carbonate concentration, as evinced earlier in the current density discrepancy in Fig. 3 at -1.5 V. The CO_2 utilisation also reaches a minimum, despite continually increasing pH, as the decreasing Faradaic efficiency indicates that the HER is beginning to dominate.
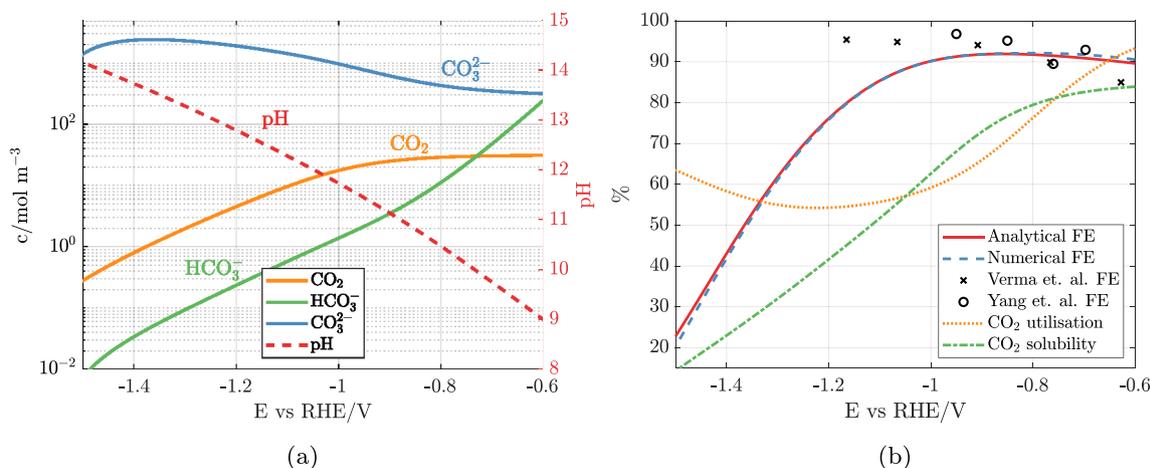
Fig. 6. Analytical plots against cathode potential of Faradaic efficiency, defined as the percentage of electrons used to reduce CO_2 to CO, along with the Faradaic efficiencies corresponding to the experimental results in Fig. 3a, and analytical CL averaged aqueous concentrations as a function of potential(b). Additionally plotted in (a) are curves for CO_2 utilisation, defined as the percentage of CO_2 entering from the GDL that is converted to CO, and CO_2 solubility in the CL catholyte, expressed as a percentage of CO_2 solubility in the bulk flow channel electrolyte.

Due to the difference in Tafel slopes, at more negative potentials HER will never produce enough OH^- to consume CO_2 faster than the electrode, and CO_2 utilisation will converge to 100%, despite the FE converging to 0%. Although the FE prediction is a reasonable match to the experimental data at small potentials, the decrease at potentials lower than -1 V is not seen experimentally. This is most likely due to the suppression of HER at high pH [21], which is not included in the Tafel kinetics implemented in the model.

4. Conclusions

In this work we have developed an analytical approximation of CO_2 reduction in the cathodic CL. By assuming approximately homogeneous electrolyte potential in the CL and reducing the simplified mass transport of ions within the CL to a system of concentration averaged mass balance equations, we derived a simple system of equations that capture the effects of the chemical reaction of CO_2 with OH^-, the carbonate equilibrium reactions, the concentration dependent CO_2 electroreduction kinetics, and the CO_2 solubility reduction at high ionic strengths. The accuracy of the model was demonstrated through comparison to experimental and numerical results for CO current density and spatial CO_2 concentration variation respectively. The model was shown to correctly predict CL performance in both activation overpotential limited regimes and mass-transfer limited regimes, and transition smoothly between the two. The model predicts limiting current densities from mass-transfer and homogeneous reaction limitations, though it must be noted that these predictions may exceed attainable current densities in cells prone to liquid breakthrough, precipitation, or other stability issues, with additional limitations addressed in SI.6.

Transport and reaction interplay in the CL has been covered by a number of numerical studies, but with this work we demonstrated that this behaviour can be approximated analytically to a similar degree of complexity. This should motivate future numerical studies to focus either on including more detailed physics within the CL or expanding the scope to include more influence from the diffusion medium or electrolyte channel. For instance, we assume that the MPL remains entirely dry at all potentials, despite the adjacent CL being entirely flooded, and this lets the model predict high current densities that may not be possible for a physical cell to achieve without flooding.

We assumed simple kinetics for the heterogeneous reactions, and although this is still common, the model of Weng et al.

[51] utilises a more involved description for kinetic parameters and better captures the suppression of the HER at high pH. We expect that the inclusion of such an effect would better the agreement of the model with the Faradaic efficiencies reported in Fig. 6b. Similarly, the Smith group note that catalyst studies are often performed in conditions that are unrealistic for commercial use[15], such as weak electrolytes or low current densities, and as such modelling studies are forced to broadly extrapolate from kinetic data. Future endeavours to extract kinetic parameters from experimental data should also similarly account for this influence of local environment on activation energy.

Although it has been commonplace to restrict numerical studies to the through-plane dimension, we herein predict that the variation of electrolyte channel concentration boundary layers alone is sufficient reason to merit the inclusion of flow-wise dimension, such as in the work of Kas et al. [39]. Weber and coworkers have already demonstrated the positive impact of pH buffering electrolytes on the limiting current density[52] and we herein show that these improvements can be magnified by increasing flow rate. Increasing buffer strength will increase CO_2 utilisation and limiting current density, but the corresponding decrease in CO_2 solubility will lead to a decrease in current density unless counteracted with increased partial pressure, and higher ionic strengths could lead to earlier onset of precipitation events. It would be of great use to future numerical studies if experimental studies would report channel dimensions along with flow-rates, as the latter alone are insufficient to determine boundary layer profiles. Like other studies we predict significant carbonate formation in the CL, so further work should investigate the effect of the migration of this carbonate to the anode and how it could accumulate in a recycled electrolyte. Carbonate crossover is difficult to prevent, and research from the Chiu group has shown that the anion-exchange membranes exhibit a strong bias towards the transport of carbonate[53], due to its higher valence, and their resistances also increase as a consequence[54]. At high current densities we also predict an increase in electrolyte ionic strength, the effects of which are manifold. Most of these effects are neglected in this approximation and many other numerical studies, but the large effect of salting-out alone shows that, in agreement with the recommendations of Nesbitt and Smith [55], high ionic strength effects are imperative to include in future studies, particularly with regards to solubility and chemical activity. Ionic strength corrections are often entirely empirical or complicated in form, necessitating numerical approaches. If they are neglected then full numerical modelling is likely to be

unnecessary because, as we have shown in this work, the system will likely be analytically approximable.

The versatility of the analytical model allowed us to perform parametric studies over large ranges of CL thicknesses and electrolyte channel flow rates. It was shown that minimising transport resistances in both the CL and the electrolyte channel is crucial in attaining optimal CO current densities. The benefit of shorter diffusion distances and increased Faradaic efficiencies in thin CLs was shown to outweigh the reduction in reactive surface area, yielding higher CO current densities than thicker CLs at more negative potentials. The benefit of increased flow rate was also shown, as catholyte regulation is governed by electrolyte boundary mass transfer and is essential in maintaining a low pH and ionic strength within the CL. We have also given context to these results, showing that such parameter recommendations are only valid in mass transfer limited regimes and can be detrimental at less negative potentials. By providing a freely accessible spreadsheet containing the model we facilitate further independent analytical studies and hope to motivate further work in the development of practical analytical approximations for GDE design and optimisation for CO_2 reduction.

Declaration of Competing Interest

The authors declare that they have no known competing financial interests or personal relationships that could have appeared to influence the work reported in this paper.

Credit authorship contribution statement

J.W. Blake: Conceptualization, Methodology, Software, Validation, Formal analysis, Writing – original draft. **J.T. Padding:** Conceptualization, Methodology, Supervision, Funding acquisition, Writing – review & editing. **J.W. Haverkort:** Conceptualization, Methodology, Supervision, Funding acquisition, Writing – review & editing.

Acknowledgements

Supplementary material

Supplementary material associated with this article can be found, in the online version, at doi:10.1016/j.electacta.2021.138987.

References

[1] Z. Yan, J.L. Hitt, J.A. Turner, T.E. Mallouk, Renewable electricity storage using electrolysis, Proc. Natl. Acad. Sci. 117 (23) (2020) 12558–12563, doi:10.1073/pnas.1821686116. https://www.pnas.org/content/117/23/12558

[2] W. Smith, T. Burdyny, D. Vermaas, H. Geerlings, Pathways to industrial-scale fuel out of thin air from CO_2 electrolysis, Joule 3 (8) (2019) 1822–1834, doi:10.1016/j.joule.2019.07.009.

[3] S. van Bavel, S. Verma, E. Negro, M. Bracht, Integrating CO_2 electrolysis into the gas-to-liquids-power-to-liquids process, ACS Energy Lett. 5 (8) (2020) 2597–2601, doi:10.1021/acsenergylett.0c01418.

[4] H.L. Tuller, Solar to fuels conversion technologies: a perspective, Mater. Renew. Sustain. Energy 6 (1) (2017) 3, doi:10.1007/s40243-017-0088-2.

[5] H. Xiang, H.A. Miller, M. Bellini, H. Christensen, K. Scott, S. Rasul, E.H. Yu, Production of formate by CO_2 electrochemical reduction and its application in energy storage, Sustain. Energy Fuels 4 (2020) 277–284, doi:10.1039/C9SE00625G.

[6] A.S. Agarwal, Y. Zhai, D. Hill, N. Sridhar, The electrochemical reduction of carbon dioxide to formate/formic acid: engineering and economic feasibility, ChemSusChem 4 (9) (2011) 1301–1310, doi:10.1002/cssc.201100220.

[7] S. Hernández, M. Amin Farkhondehfal, F. Sastre, M. Makkee, G. Saracco, N. Russo, Syngas production from electrochemical reduction of CO_2: current status and prospective implementation, Green Chem. 19 (2017) 2326–2346, doi:10.1039/C7GC00398F.

[8] E. Andreoli, CO_2-to-ethylene electroreduction gets a boost, Nat Catal. 4 (1) (2021) 8–9, doi:10.1038/s41929-020-00568-9.

[9] M. Gattrell, N. Gupta, A. Co, Electrochemical reduction of CO_2 to hydrocarbons to store renewable electrical energy and upgrade biogas, Energy Convers. Manage. 48 (4) (2007) 1255–1265, doi:10.1016/j.enconman.2006.09.019.

[10] D. Pabsch, C. Held, G. Sadowski, Modeling the CO_2 solubility in aqueous electrolyte solutions using ePC-SAFT, J. Chem. Eng. Data 65 (12) (2020) 5768–5777, doi:10.1021/acs.jced.0c00704.

[11] C. Delacourt, P.L. Ridgway, J. Newman, Mathematical modeling of CO_2 reduction to CO in aqueous electrolytes, J. Electrochem. Soc. 157 (12) (2010) B1902, doi:10.1149/1.3502532.

[12] M.-Y. Lee, K.T. Park, W. Lee, H. Lim, Y. Kwon, S. Kang, Current achievements and the future direction of electrochemical CO_2 reduction: a short review, Crit. Rev. Environ. Sci.Technol. 50 (8) (2020) 769–815, doi:10.1080/10643389.2019.1631991.

[13] M. Paidar, V. Fateev, K. Bouzek, Membrane electrolysis-history, current status and perspective, Electrochim. Acta 209 (2016) 737–756, doi:10.1016/j.electacta.2016.05.209.

[14] D. Wu, Review of system integration and control of proton exchange membrane fuel cells, Electrochem. Energ. Rev. 3 (2020) 466–505, doi:10.1007/s41918-020-00068-1.

[15] T. Burdyny, W.A. Smith, CO_2 reduction on gas-diffusion electrodes and why catalytic performance must be assessed at commercially-relevant conditions, Energy Environ. Sci. 12 (2019) 1442–1453, doi:10.1039/C8EE03134G.

[16] J. Zhou, S. Shukla, A. Putz, M. Secanell, Analysis of the role of the microporous layer in improving polymer electrolyte fuel cell performance, Electrochim. Acta 268 (2018) 366–382, doi:10.1016/j.electacta.2018.02.100. http://www.sciencedirect.com/science/article/pii/S0013468618304043

[17] Y. Chen, N.S. Lewis, C. Xiang, Modeling the performance of a flow-through gas diffusion electrode for electrochemical reduction of CO or CO_2, J. Electrochem. Soc. 167 (11) (2020) 114503, doi:10.1149/1945-7111/ab987a.

[18] Q. Wang, H. Dong, H. Yu, H. Yu, Enhanced performance of gas diffusion electrode for electrochemical reduction of carbon dioxide to formate by adding polytetrafluoroethylene into catalyst layer, J. Power Sources 279 (2015) 1–5, doi:10.1016/j.jpowsour.2014.12.118. http://www.sciencedirect.com/science/article/pii/S0378775314021570

[19] M. Leonard, L. Clarke, A. Forner-Cuenca, S. Brown, F. Brushett, Investigating electrode flooding in a flowing electrolyte, gas-fed carbon dioxide electrolyzer, ChemSusChem 13 (2019) 400–411, doi:10.1002/cssc.201902547.

[20] A. Goyal, G. Marcandalli, V.A. Mints, M.T.M. Koper, Competition between CO_2 reduction and hydrogen evolution on a gold electrode under well-defined mass transport conditions, J. Am. Chem. Soc. 142 (9) (2020) 4154–4161, doi:10.1021/jacs.9b10061.

[21] B. Kim, S. Ma, H.-R. Molly Jhong, P.J. Kenis, Influence of dilute feed and ph on electrochemical reduction of CO_2 to CO on ag in a continuous flow electrolyzer, Electrochim. Acta 166 (2015) 271–276, doi:10.1016/j.electacta.2015.03.064. http://www.sciencedirect.com/science/article/pii/S0013468615006465

[22] M. Sechenov, On the behavior of salt solutions based on their relation to carbon dioxide, Z. Phys. Chem. (1889) 117–125.

[23] J. Zhang, W. Luo, A. Züttel, Crossover of liquid products from electrochemical CO_2 reduction through gas diffusion electrode and anion exchange membrane, J. Catal. 385 (2020) 140–145, doi:10.1016/j.jcat.2020.03.013. https://www.sciencedirect.com/science/article/pii/S0021951720300968

[24] J. Herranz, A. Pătru, E. Fabbri, T.J. Schmidt, Co-electrolysis of CO_2 and H_2O: from electrode reactions to cell-level development, Curr. Opin. Electrochem. 23 (2020) 89–95, doi:10.1016/j.coelec.2020.05.004. https://www.sciencedirect.com/science/article/pii/S2451910320301046

[25] S. Erbach, S. Epple, M. Heinen, G. Toth, M. Klages, D. Gaudreau, M. Ages, A. Putz, CO_2 enrichment in anode loop and correlation with CO poisoning of Low Pt Anodes in PEM Fuel Cells, Fuel Cells 18 (5) (2018) 613–618, doi:10.1002/fuce.201700216.

[26] S. Zhao, R. Jin, R. Jin, Opportunities and challenges in CO_2 reduction by gold- and silver-based electrocatalysts: From bulk metals to nanoparticles and atomically precise nanoclusters, ACS Energy Lett. 3 (2) (2018) 452–462, doi:10.1021/acsenergylett.7b01104.

[27] A. Goyal, G. Marcandalli, V.A. Mints, M.T.M. Koper, Competition between CO_2 reduction and hydrogen evolution on a gold electrode under well-defined mass transport conditions, J. Am. Chem. Soc. 142 (9) (2020) 4154–4161, doi:10.1021/jacs.9b10061.

[28] J.W. Vickers, D. Alfonso, D.R. Kauffman, Electrochemical carbon dioxide reduction at nanostructured gold, copper, and alloy materials, Energy Technol. 5 (6) (2017) 775–795, doi:10.1002/ente.201600580.

[29] S. Verma, X. Lu, S. Ma, R.I. Masel, P.J.A. Kenis, The effect of electrolyte composition on the electroreduction of CO_2 to CO on Ag based gas diffusion electrodes, Phys. Chem. Chem. Phys. 18 (2016) 7075–7084, doi:10.1039/C5CP05665A.

[30] Y. Hori, R. Takahashi, Y. Yoshinami, A. Murata, Electrochemical reduction of CO at a copper electrode, J. Phys. Chem. B 101 (36) (1997) 7075–7081, doi:10.1021/jp970284i.

[31] T. Yamamoto, D. Tryka, K. Hashimoto, A. Fujishima, M. Okawa, Electrochemical reduction of CO_2 in micropores, Adv. Chem. Convers. Mitigating Carbon Dioxide (1998) 585–588, doi:10.1016/S0167-2991(98)80827-6.

[32] J. Li, G. Chen, Y. Zhu, Z. Liang, A. Pei, C.-L. Wu, H. Wang, H.R. Lee, K. Liu, S. Chu, Y. Cui, Efficient electrocatalytic CO$_2$ reduction on a three-phase interface, Nat. Catal. 1 (8) (2018) 592–600, doi:10.1038/s41929-018-0108-3.

[33] N.T. Nesbitt, T. Burdyny, H. Simonson, D. Salvatore, D. Bohra, R. Kas, W.A. Smith, Liquid-solid boundaries dominate activity of CO$_2$ reduction on gas-diffusion electrodes, ACS Catal. 10 (23) (2020) 14093–14106, doi:10.1021/acscatal.0c03319.

[34] N. Ramaswamy, W. Gu, J.M. Ziegelbauer, S. Kumaraguru, Carbon support microstructure impact on high current density transport resistances in PEMFC cathode, J. Electrochem. Soc. 167 (6) (2020) 064515, doi:10.1149/1945-7111/ab819c.

[35] A. Zlotorowicz, K. Jayasayee, P. Dahl, M. Thomassen, S. Kjelstrup, Tailored porosities of the cathode layer for improved polymer electrolyte fuel cell performance, J. Power Sources 287 (2015) 472–477, doi:10.1016/j.jpowsour.2015.04.079. http://www.sciencedirect.com/science/article/pii/S0378775315007363

[36] T. Hattori, R. Miura, H. Tsuboi, N. Hatakeyama, H. Takaba, M. Williams, A. Miyamoto, Porosity and Pt content in the catalyst layer of PEMFC: effects on diffusion and polarization characteristics, Int. J. Electrochem. Sci. 5 (2010) 2221–2229.

[37] C. Lee, B. Zhao, J.K. Lee, K.F. Fahy, K. Krause, A. Bazylak, Bubble formation in the electrolyte triggers voltage instability in CO$_2$ electrolyzers, iScience 23 (5) (2020) 101094, doi:10.1016/j.isci.2020.101094. https://www.sciencedirect.com/science/article/pii/S2589004220302790

[38] S. Weisenberger, A. Schumpe, Estimation of gas solubilities in salt solutions at temperatures from 273 K to 363 K, Aiche J. 42 (1996) 298–300.

[39] R. Kas, A.G. Star, K. Yang, T. Van Cleve, K.C. Neyerlin, W.A. Smith, Along the channel gradients impact on the spatioactivity of gas diffusion electrodes at high conversions during CO$_2$ electroreduction, ACS Sustain. Chem. Eng. 9 (3) (2021) 1286–1296, doi:10.1021/acssuschemeng.0c07694.

[40] Y. Hori, Electrochemical CO$_2$ reduction on metal electrodes, Mod. Aspects Electrochem. (2008) 89–189, doi:10.1007/978-0-387-49489-0_3.

[41] N. Dubouis, A. Grimaud, The hydrogen evolution reaction: from material to interfacial descriptors, Chem. Sci. 10 (2019) 9165–9181, doi:10.1039/C9SC03831K.

[42] E.W. Thiele, Relation between catalytic activity and size of particle, Ind. Eng. Chem. 31 (7) (1939) 916–920, doi:10.1021/ie50355a027.

[43] T. Hatsukade, K.P. Kuhl, E.R. Cave, D.N. Abram, T.F. Jaramillo, Insights into the electrocatalytic reduction of CO$_2$ on metallic silver surfaces, Phys. Chem. Chem. Phys. 16 (2014) 13814–13819, doi:10.1039/C4CP00692E.

[44] J. Newman, K.E. Thomas-Alyea, Electrochemical Systems, John Wiley & Sons, 2012.

[45] L.-C. Weng, A.T. Bell, A.Z. Weber, Modeling gas-diffusion electrodes for CO$_2$ reduction, Phys. Chem. Chem. Phys. 20 (2018) 16973–16984, doi:10.1039/C8CP01319E.

[46] T. Soboleva, X. Zhao, K. Malek, Z. Xie, T. Navessin, S. Holdcroft, On the micro-, meso-, and macroporous structures of polymer electrolyte membrane fuel cell catalyst layers, ACS Appl. Mater. Interfaces 2 (2) (2010) 375–384, doi:10.1021/am900600y.

[47] D.T. Whipple, E.C. Finke, P.J.A. Kenis, Microfluidic reactor for the electrochemical reduction of carbon dioxide: the effect of pH, Electrochem. Solid-State Lett. 13 (9) (2010) B109, doi:10.1149/1.3456590.

[48] S. Verma, Y. Hamasaki, C. Kim, W. Huang, S. Lu, H.-R.M. Jhong, A.A. Gewirth, T. Fujigaya, N. Nakashima, P.J.A. Kenis, Insights into the low overpotential electroreduction of CO$_2$ to CO on a supported gold catalyst in an alkaline flow electrolyzer, ACS Energy Lett. 3 (1) (2018) 193–198, doi:10.1021/acsenergylett.7b01096.

[49] K. Yang, R. Kas, W.A. Smith, T. Burdyny, Role of the carbon-based gas diffusion layer on flooding in a gas diffusion electrode cell for electrochemical CO$_2$ reduction, ACS Energy Lett. 6 (1) (2021) 33–40, doi:10.1021/acsenergylett.0c02184.

[50] J.W. Haverkort, A theoretical analysis of the optimal electrode thickness and porosity, Electrochim. Acta 295 (2019) 846–860, doi:10.1016/j.electacta.2018.10.065. https://www.sciencedirect.com/science/article/pii/S0013468618323041

[51] L.-C. Weng, A.T. Bell, A.Z. Weber, Towards membrane-electrode assembly systems for CO$_2$ reduction: a modeling study, Energy Environ. Sci. 12 (2019) 1950–1968, doi:10.1039/C9EE00909D.

[52] H. Hashiba, L.-C. Weng, Y. Chen, H.K. Sato, S. Yotsuhashi, C. Xiang, A.Z. Weber, Effects of electrolyte buffer capacity on surface reactant species and the reaction rate of CO2 in electrochemical CO2 reduction, J. Phys. Chem. C 122 (7) (2018) 3719–3726, doi:10.1021/acs.jpcc.7b11316.

[53] A.M. Kiss, T.D. Myles, K.N. Grew, A.A. Peracchio, G.J. Nelson, W.K.S. Chiu, Carbonate and bicarbonate ion transport in alkaline anion exchange membranes, J. Electrochem. Soc. 160 (9) (2013) F994–F999, doi:10.1149/2.037309jes.

[54] J.A. Wrubel, A.A. Peracchio, B.N. Cassenti, T.J. Omasta, W.E. Mustain, K.N. Grew, W.K.S. Chiu, Predicting the effects of carbon dioxide on the conductivity of electrospun anion exchange membranes, J. Electrochem. Soc. 166 (14) (2019) F1047–F1054, doi:10.1149/2.0481914jes.

[55] N. Nesbitt, W. Smith, Water activity regulates CO$_2$ reduction in gas-diffusion electrodes, 202110.26434/chemrxiv.13571141.v1